Passivity Fractional-Order Sliding-Mode Control of Grid-Connected Converter With *LCL* Filter

Bo Long, *Senior Member, IEEE*, WenZe Mao, PengJie Lu, Jose Rodriguez, *Life Fellow, IEEE*, Josep M. Guerrero, *Fellow, IEEE*, Kil To Chong, *Member, IEEE*, and YunLong Teng

***Abstract*—Grid-connected converter with *LCL* filter plays an important role in renewable power generation systems. However, existing control techniques face several challenges in practice (e.g., difficulty in parameter design, slow dynamic response, and poor robustness under slowly time-varying filter parameter, deadtime of power devices, and external disturbances). To solve these difficulties, a passivity-based fractional-order sliding-mode control (PBC-FOSMC) hybrid controller, which combines the merits of passivity-based control (PBC) and FOSMC, is proposed, where the inputs of the passive controller are the outputs of the FOSMC controller. First, a passive current controller is designed based on the Euler–Lagrange model established by damping injection according to the PBC theory, which can make the system automatically converge to meet the energy dissipation law. Second, an FOSMC controller is designed to further enhance the system robustness to counter disturbances and compensate the reference current accuracy of PBC. The introduced fractional order can successfully suppress the undesired chattering due to the switching behaviors in conventional sliding-mode control. Third, the hybrid PBC-FOSMC controller is derived and system stability is analyzed. Finally, experimental results under 10-kW prototype validate the excellent performance of the proposed method in terms of robustness, dynamic performance, strong perturbation rejection ability, etc., and the desired control targets are achieved.**

***Index Terms*—Euler–Lagrange (EL) model, fractional order, grid-connected converter (GCC), *LCL* filter, passivity-based control (PBC), sliding-mode control (SMC).**

Manuscript received 27 July 2022; revised 22 November 2022 and 8 January 2023; accepted 10 February 2023. Date of publication 15 February 2023; date of current version 20 April 2023. This work was supported in part by the Fundamental Research Funds for the Central Universities of China under Grant ZYGX2019J033, in part by the Natural Science Foundation of Sichuan Province under Grant 23NSFSC0439, in part by the Key Laboratory of Special Machine and High Voltage Apparatus, Shenyang University of Technology, Ministry of Education under Grant KFKT202206, in part by the Guangdong Basic and Applied Basic Research Foundation under Grant 2021A1515010666, and in part by the VELUX FOUNDATIONS under the VILLUM Investigator Grant Center for Research on Microgrids (25920). Recommended for publication by Associate Editor Y. Xue. *(Corresponding author: YunLong Teng.)*

Bo Long, WenZe Mao, and PengJie Lu are with the School of Mechanical and Electrical Engineering, Institute for Electric Vehicle Driving System and Safety Technology, University of Electronic Science and Technology of China, Chengdu 611731, China, also with the Yangtze Delta Region Institute (Huzhou), University of Electronic Science and Technology of China, Huzhou 313001, China, also with the Institute of Electronic and Information Engineering, University of Electronic Science and Technology of China, Dongguan 523808, China, and also with the MOE Key Laboratory of Special Machine and High Voltage Apparatus, Shenyang University of Technology, Shenyang 110870, China (e-mail: longbouestc1980@126.com; 330319886@qq.com; 201952040610@std.uestc.edu.cn).

Jose Rodriguez is with the Faculty of Engineering, Universidad Andres Bello, Santiago 8370146, Chile (e-mail: jose.rodriguez@unab.cl).

Josep M. Guerrero is with the Department of Energy Technology, Aalborg University, DK-9220 Aalborg, Denmark (e-mail: joz@et.aau.dk).

Kil To Chong is with the Department of Electronics and Information Engineering, Jeonbuk National University, Jeonju 54896, South Korea (e-mail: kitchong@jbnu.ac.kr).

YunLong Teng is with the School of Mechanical and Electrical Engineering, University of Electronic Science and Technology of China, Chengdu 611731, China (e-mail: ylteng@uestc.edu.cn).

Color versions of one or more figures in this article are available at https://doi.org/10.1109/TPEL.2023.3244754.

Digital Object Identifier 10.1109/TPEL.2023.3244754

I. Introduction

With the rapid development of renewable energy sources, the requirement of power quality and stability of grid-connected converters (GCC) have become more stringent. Owing to the key characteristics of GCC, an increasing number of researchers study it [1], [2]. An important goal of the control engineer is to suppress chaotic oscillations or reduce unnecessary fluctuations and achieve high-quality grid current integration. According to standards, such as IEEE 519-1992 and IEEE 1547-2008 [3], the total harmonic distortion (THD) of the current injected into the power grid should not exceed 5% of the rated current. Moreover, each current harmonic higher than the 35th harmonic should be limited to less than 0.3% of the rated fundamental current. Therefore, an effective control strategy for the current regulators is of great significance.

Compared with the conventional *L* filter, the *LCL* filter has a better harmonic attenuation capability and lower cost [4], which has drawn much attention and has been widely used. However, two additional complex conjugate poles in the *LCL* filter may lead to system instability. In addition, the main source of *LCL* filter uncertainties is the grid impedance, which may deteriorate the system performance or even lead to unstable operation. All of these requirements may challenge the controller design to achieve high-quality grid current injection, resonance damping, low THD, fast dynamic response, and strong system stability [5].

Many control strategies for GCC with LCL filter (*LCL*-GCC) have been studied. The existing active damping control strategies for *LCL*-GCC include proportional integral (PI) control [6], [7], proportional-resonance (PR) control [8], repetitive control (RC) [9], and deadbeat control methods [10]. The PI algorithm is the most widely used method, and is characterized by a simple structure, easy implementation, and independence from the mathematical model of the control object [11]. However, it is sensitive to interference, poor tracking ability for time-varying ac signals, and steady-state error in inverter control [12]. PR control has no steady-state error in tracking time-varying ac

signals and can obtain infinite gain at the fundamental frequency [13], [14]. However, the PR may deteriorate in stability as the line impedance increases [15]. Moreover, it is sensitive to changes in parameters. The RC control method has an excellent effect on the processing of periodic signals. However, it requires a high-precision and accurate system model and is sensitive to external interference. Therefore, RC is typically combined with other methods for improvement [16].

In addition to traditional linear controllers, nonlinear control strategies have been studied to obtain more robust performance. Compared to traditional methods, nonlinear control [i.e., sliding-mode control (SMC), model predictive control (MPC), and H_∞ control] has an excellent effect in dealing with complex environments. In [17], a robust adaptive voltage control method was proposed for a three-phase inverter, which has a strong robustness to system uncertainties. The system performance can be improved by adaptively selecting the control mode according to the working conditions. However, owing to its complex mathematical model, adaptive control is difficult to implement in engineering. In [18], an H_∞ controller with explicit robustness in terms of grid impedance variations was proposed to incorporate the desired tracking performance and stability margin. However, the weight function has to rely on designer experience, the algorithm is complex, and it is difficult to implement in an actual system. Wai et al. [19] developed two newly designed control strategies for a single-stage boost inverter: an adaptive control scheme and a fuzzy neural network control system. It has an excellent control effect on the nonlinear loads. However, there is no general method or theory to select the appropriate fuzzy rules, and the complexity of the model creates tradeoffs that hinder its generalization ability. The aforementioned nonlinear control methods improve the performance of the system in some way; however, they do not fundamentally solve the problem of robust disturbance rejection.

Passivity-based control (PBC) is a nonlinear control strategy based on the concept of energy. It has the advantages of high stability and robustness, and the algorithm design is simple and easy to implement. Therefore, it is suitable for industrial control applications with complex environments and fluctuating parameters [20], [21], [22]. The passive controller design mainly makes the closed-loop system passive by injecting damping into the system so that the energy function of the system converges to the expected energy function; thus, the error between the controlled system state and the expected state can gradually converge to zero [23]. Therefore, if the system is strictly passive, it will always maintain global stability. Therefore, passive control is robust to system-parameter fluctuations and external interference.

As long as the system features passivity, it maintains global stability. Therefore, passive control is robust to variations in system parameters and external interference. Because of its excellent robustness, stability, and easy realization, it has been widely used in industry. In [24], improved passivity control based on energy shaping and damping injection was proposed for a single-phase uninterruptible power supply. As long as the inductor current tracks its reference, output voltage control can be realized indirectly on the premise that the inductor current tracks its reference. However, the estimated parameters often do not match actual parameters. To solve this problem, a voltage outer loop was added to the traditional passive control, which significantly increased the robustness to large-scale parameter excuse. In [25], a passivity model prediction scheme for a three-level neutral-point-clamped (NPC) inverter-fed induction motor was proposed. To solve the problem in which the performance of finite control set MPC (FCS-MPC) is highly dependent on accurate measurement and parameter estimation, a passive model predictive scheme was proposed. Because the power shaping and damping injection of the proposed scheme inherit passive control, it improves the robustness under inevitable measurement noise interference and parameter change. In [26], a simplified parallel-damped passivity-based controller was proposed for a dc–dc boost converter to eliminate steady-state errors caused by parasitic resistance so that the highly nonlinear dc–dc boost converter has strong robustness to load changes. In [27], to address the instability of a dc–dc buck power converter under a constant power load in a dc microgrid, a robust nonlinear control strategy based on passivity was proposed. Based on the PBC, a nonlinear disturbance observer was added to ensure high signal stability and rapid recovery performance of the system during disturbance and uncertainty. This improved the robustness of the system to load changes. In [28], a decoupling control scheme based on passivity was proposed for a T-type NPC photovoltaic (PV) grid-connected inverter. A passivity controller was designed using the damping injection method. The grid-connected inverter for PV based on passivity has strong robustness to disturbances and can effectively suppress the influence of the delay in the inverter.

The motivations of this article are given as follows. First, although passive control is widely used in the industry because of its simple design and good robustness, it still requires an accurate system model, and the uncertain parameters in the system operation affect the balance point, which has a negative impact on the control performance of the controller. Fractional-order SMC (FOSMC) has the advantages of strong robustness against external disturbances (e.g., grid voltage variations) and internal filter parameter variations, because of the fractional sliding surface, FOSMC controller has much smaller chattering compared with SMC controller [29], [30]. Therefore, the combination of FOSMC and passive control (PBC-FOSMC) solves the problem of passive control requiring highly accurate system parameters, endowing the entire system with the characteristics of fast response speed and insensitivity to filter parameter changes and external disturbances, thus the robust passivity stability of the system is enhanced. Second, in the proposed PBC-FOSMC, fractional-order theory is introduced to design the sliding surface, making the system state smoother when it approaches the sliding surface so that the chattering that originally converges along the sliding surface can be maximally suppressed. In summary, the main contributions of this study are as follows.

1) Based on the power circuit and operating principles of an *LCL*-GCC filter, a hybrid controller PBC-FOSMC that

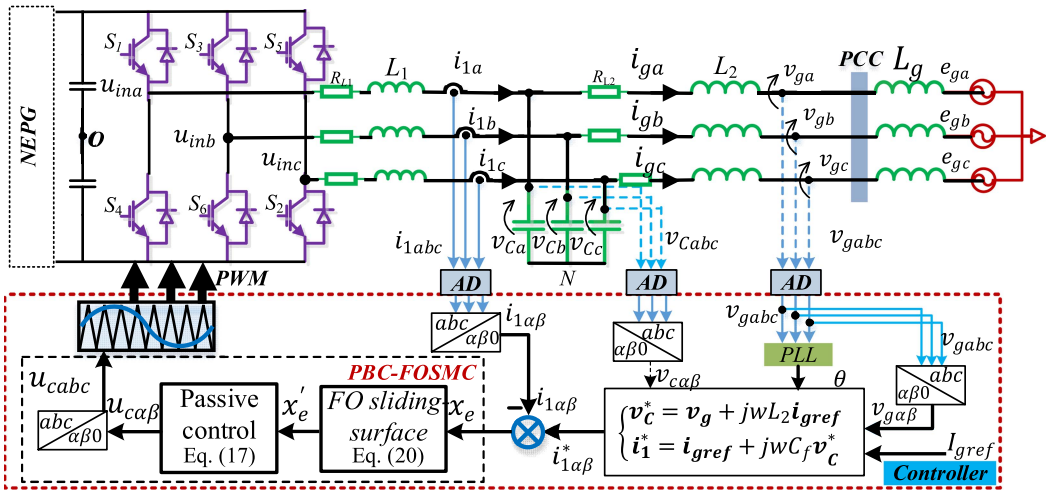

Fig. 1. Block diagram of NEPG system with PBC-FOSMC controller.

combines SMC control with PBC control is introduced, which causes the system to converge to the equilibrium point along the sliding surface while maintaining passivity. Through damping injection, the proposed PBC-FOSMC controller further enhances the system robustness against disturbances.

2) The fractional sliding surface is introduced into the passive control to make the motion of the system state gently approach the sliding surface, which can suppress the chattering, thus improving the quality of the grid current.
3) The digital control law of the PBC-FOSMC controller is derived, and a stability analysis is demonstrated. Finally, the effectiveness of the proposed scheme under four typical scenarios is illustrated through an experiment with a 10-kW prototype.

The remaining of this article is as follows. Section II introduces the system structure and its challenges. Section III introduces the modeling of *LCL*-GCC and its passivity analysis. Section IV presents the design of the hybrid controller, including the design of the inner-loop passive current controller, outer-loop FOSMC controller, PBC-FOSMC controller, and its digitalization. Section V analyzes system stability. In Section VI, the effectiveness of the proposed control method over existing techniques is experimentally verified. Finally, Section VII concludes this article.

II. Structure of an *LCL*-GCC System and Modeling

A. System Description

In practical applications, a new energy power generation (NEPG) system is necessary to achieve good robustness to external and internal parameter disturbances. Fig. 1 shows the proposed PBC-FOSMC strategy for a PV grid-connected system. The output of the PV array voltage is transformed into the input dc-link voltage of the *LCL*-GCC via a dc–dc converter. The dc-link voltage is changed to ac voltage, which is further filtered by an *LCL* filter required for grid integration.

The operating principles of the control system are briefly described as follows.

First, the reference grid current and grid voltage sampled are input into the reference calculation module, with the help of a phase-lock-loop (PLL) module, the reference inverter-side current i_1^* is obtained and then a difference with the actual inverter current is calculated to obtain the current tracking error. It is needed to note that, during the modeling analysis, the grid conditions are assumed to be ideal, thus, the PLL can maintain its stable operation and generates accurate frequency and phase references for the *LCL*-GCC converter, and there are no stability issues caused by the interactions between PLL and the grid impedance [31], [32], [33].

Second, the inverter current error converges on the fractional sliding surface through the SMC module. The system state is then inputted to the passive controller. Thus, the system not only has passivity but also sliding-mode characteristics because the system state converges along the sliding surface.

Finally, the output control law of the PBC controller is inputted to the pulsewidth modulation block.

B. Problem Description

For the *LCL*-GCC system to maintain system stability and guarantee high-quality grid current integration, there are several challenges. First, owing to temperature changes, the filter parameters may also vary, which may lead to modeling errors and deteriorate the grid current quality. In addition, the time delay in gate-driving and unknown grid impedance under weak grid conditions may both endanger system stability. Second, in addition to internal disturbances, there are also some external disturbances, for example, dc-ink voltage variations, abrupt grid voltage, and load changes. All of these factors may influence the steady-state and dynamic response of the grid current. Therefore, a control solution that guarantees the system stability, robustness, dynamic response, and quality of the grid current should be considered.

III. Mathematical Model and Passivity Analysis of an *LCL*-GCC System

A. Power Circuit and Euler–Lagrange (EL) Model of LCL-GCC

As shown in Fig. 1, the power circuit of a two-level *LCL*-GCC system consists of a three-phase inverter, *LCL* filters, and an ac grid. The dc-link voltage may originate from renewable energy sources (e.g., PV and wind power generation). The *LCL*-GCC system may function as a current- or voltage-controlled voltage source converter (VSC). In Fig. 1, the inductances of the converter- and grid-side inductors are denoted by $\boldsymbol{L}_1$ and $\boldsymbol{L}_2$. The filter capacitance of *LCL* filter is denoted by $\boldsymbol{C_f}$; the output three-phase voltages of the inverter are $\boldsymbol{u_{ina}}$, $\boldsymbol{u_{inb}}$, and $\boldsymbol{u_{inc}}$; the output three-phase converter-side currents of the inverter are $\boldsymbol{i_{1a}}$, $\boldsymbol{i_{1b}}$, and $\boldsymbol{i_{1c}}$; the output three-phase grid-side currents of the inverter are $\boldsymbol{i_{2a}}$, $\boldsymbol{i_{2b}}$, and $\boldsymbol{i_{2c}}$; the voltages of $\boldsymbol{C_f}$ are $\boldsymbol{u_{ca}}$, $\boldsymbol{u_{cb}}$, and $\boldsymbol{u_{cc}}$; the three-phase PCC voltages of the grid are $\boldsymbol{v_{ga}}$, $\boldsymbol{v_{gb}}$, and $\boldsymbol{v_{gc}}$; the three-phase grid voltages are $\boldsymbol{e_{ga}}$, $\boldsymbol{e_{gb}}$, and $\boldsymbol{e_{gc}}$. $\boldsymbol{R_{L1}}$ and $\boldsymbol{R_{L2}}$ are the parasitic resistance of the inductors $\boldsymbol{L}_1$ and $\boldsymbol{L}_2$. It is assumed that the three-phase voltages of the grid are balanced, and the modeling of the LCC-GCC with variables is set up, as shown in Fig. 1.

To reduce the number of control variables, the controller is designed in $\alpha\beta$-coordinate, and all subsequent calculations are also in the stationary $\alpha\beta$-coordinate frame. According to Kirchhoff's law, the voltage and current equation under $\alpha\beta$-coordinates by Clarke transformation can be derived as

$$\begin{cases} \begin{bmatrix} \dot{i}_{1\alpha} \\ \dot{i}_{1\beta} \end{bmatrix} = -\frac{R_{L1}}{L_1}\begin{bmatrix} i_{1\alpha} \\ i_{1\beta} \end{bmatrix} - \frac{1}{L_1}\begin{bmatrix} v_{c\alpha} \\ v_{c\beta} \end{bmatrix} + \frac{1}{L_1}\begin{bmatrix} u_{in\alpha} \\ u_{in\beta} \end{bmatrix} \\ \begin{bmatrix} \dot{i}_{g\alpha} \\ \dot{i}_{g\beta} \end{bmatrix} = -\frac{R_{L2}}{L_2}\begin{bmatrix} i_{g\alpha} \\ i_{g\beta} \end{bmatrix} + \frac{1}{L_2}\begin{bmatrix} v_{c\alpha} \\ v_{c\beta} \end{bmatrix} - \frac{1}{L_2}\begin{bmatrix} v_{g\alpha} \\ v_{g\beta} \end{bmatrix} \\ \begin{bmatrix} \dot{\mathrm{v}}_{c\alpha} \\ \dot{\mathrm{v}}_{c\beta} \end{bmatrix} = \frac{1}{C_f}\begin{bmatrix} i_{1\alpha} \\ i_{1\beta} \end{bmatrix} - \frac{1}{C_f}\begin{bmatrix} i_{g\alpha} \\ i_{g\beta} \end{bmatrix} \end{cases}. \tag{1}$$

In (1), $\boldsymbol{i}_{1\alpha\beta} = [i_{1\alpha}\ i_{1\beta}]^T$ is the inverter-side current; $\boldsymbol{v}_{C\alpha\beta} = [v_{C\alpha}\ v_{C\beta}]^T$ is the capacitance voltage; $\boldsymbol{u}_{\mathrm{in}\alpha\beta} = [u_{\mathrm{in}\alpha}\ u_{\mathrm{in}\beta}]^T$ is the inverter input voltage; $\boldsymbol{i}_{\mathrm{g}\alpha\beta} = [i_{\mathrm{g}\alpha}\ i_{\mathrm{g}\beta}]^T$ is the grid current; and $\boldsymbol{v}_{\mathrm{g}\alpha\beta} = [v_{\mathrm{g}\alpha}\ v_{\mathrm{g}\beta}]^T$ is the grid voltage. In (1), $\boldsymbol{i}_{\mathrm{g}\alpha\beta} = \boldsymbol{C}_{3s/2s}\,\boldsymbol{i}_{\mathrm{gabc}}$, $\boldsymbol{u}_{in\alpha\beta} = \boldsymbol{C}_{3s/2s}\,\boldsymbol{v}_{\mathrm{gabc}}$, $\boldsymbol{v}_{\mathrm{c}\alpha\beta} = \boldsymbol{C}_{3s/2s}\,\boldsymbol{v}_{\mathrm{cabc}}$, $\boldsymbol{v}_{\mathrm{g}\alpha\beta} = \boldsymbol{C}_{3s/2s}\ \boldsymbol{v}_{\mathrm{gabc}}$, and $\boldsymbol{i}_{1\alpha\beta} = \boldsymbol{C}_{3s/2s}\,\boldsymbol{i}_{1\mathrm{abc}}$. The Clarke transformation is given by

$$\mathbf{C}_{3\mathrm{s}/2\mathrm{s}} = \frac{2}{3}\begin{bmatrix} 1 & -0.5 & -0.5 \\ 0 & \frac{\sqrt{3}}{2} & -\frac{\sqrt{3}}{2} \end{bmatrix}.$$

To obtain the EL equation of the system, (1) can be transformed into (2), given by

$$\begin{cases} L_1\begin{bmatrix} \dot{i}_{1\alpha} \\ \dot{i}_{1\beta} \end{bmatrix} + R_{L1}\begin{bmatrix} i_{1\alpha} \\ i_{1\beta} \end{bmatrix} + \begin{bmatrix} v_{c\alpha} \\ v_{c\beta} \end{bmatrix} = \begin{bmatrix} u_{in\alpha} \\ u_{in\beta} \end{bmatrix} \\ L_2\begin{bmatrix} \dot{i}_{g\alpha} \\ \dot{i}_{g\beta} \end{bmatrix} + R_{L2}\begin{bmatrix} i_{g\alpha} \\ i_{g\beta} \end{bmatrix} + \begin{bmatrix} v_{g\alpha} \\ v_{g\beta} \end{bmatrix} = \begin{bmatrix} v_{c\alpha} \\ v_{c\beta} \end{bmatrix} \\ C_f\begin{bmatrix} \dot{v}_{c\alpha} \\ \dot{v}_{c\beta} \end{bmatrix} = \begin{bmatrix} i_{1\alpha} \\ i_{1\beta} \end{bmatrix} - \begin{bmatrix} i_{g\alpha} \\ i_{g\beta} \end{bmatrix} \end{cases}. \tag{2}$$

A passive controller is designed based on the system state equation obtained in (1). The state equation of the system needs to be transformed into an EL equation form given by

$$\boldsymbol{M}\dot{\boldsymbol{x}} + \boldsymbol{J}\boldsymbol{x} + \boldsymbol{R}\boldsymbol{x} = \boldsymbol{u}. \tag{3}$$

In (3), $\boldsymbol{M}$ is a positive definite diagonal matrix representing the energy storage of the inverter system. $\boldsymbol{J}$ is the antisymmetric matrix of the system that represents the interconnection structure within the system. $\boldsymbol{J}$ satisfies $\boldsymbol{J} = -\boldsymbol{J}^{\boldsymbol{T}}$. $\boldsymbol{R}$ is a positive-definite matrix that represents the dissipation characteristics of a system. $\boldsymbol{x}$ is the state variable. $\boldsymbol{u}$ is the energy exchange between the system and the external energy. The matrices are as follows:

$$\boldsymbol{M} = \begin{bmatrix} L_1 & 0 & 0 & 0 & 0 & 0 \\ 0 & L_1 & 0 & 0 & 0 & 0 \\ 0 & 0 & L_2 & 0 & 0 & 0 \\ 0 & 0 & 0 & L_2 & 0 & 0 \\ 0 & 0 & 0 & 0 & C_f & 0 \\ 0 & 0 & 0 & 0 & 0 & C_f \end{bmatrix},\ \boldsymbol{x} = \begin{pmatrix} i_{1\alpha} \\ i_{1\beta} \\ i_{g\alpha} \\ i_{g\beta} \\ v_{C\alpha} \\ v_{C\beta} \end{pmatrix},$$

$$\boldsymbol{u} = \begin{pmatrix} u_{in\alpha} \\ u_{in\beta} \\ -v_{g\alpha} \\ -v_{g\beta} \\ 0 \\ 0 \end{pmatrix}$$

$$\boldsymbol{J} = \begin{bmatrix} R_{L1} & 0 & 0 & 0 & 1 & 0 \\ 0 & R_{L1} & 0 & 0 & 0 & 1 \\ 0 & 0 & R_{L2} & 0 & -1 & 0 \\ 0 & 0 & 0 & R_{L2} & 0 & -1 \\ -1 & 0 & 1 & 0 & 0 & 0 \\ 0 & -1 & 0 & 1 & 0 & 0 \end{bmatrix},$$

$$\boldsymbol{R} = \begin{bmatrix} 0 & 0 & 0 & 0 & 0 & 0 \\ 0 & 0 & 0 & 0 & 0 & 0 \\ 0 & 0 & 0 & 0 & 0 & 0 \\ 0 & 0 & 0 & 0 & 0 & 0 \\ 0 & 0 & 0 & 0 & 0 & 0 \\ 0 & 0 & 0 & 0 & 0 & 0 \end{bmatrix}.$$

B. Passivity Analysis of LCL-GCC Converter

For an affine nonlinear system given by

$$\begin{cases} \dot{\boldsymbol{x}} = \boldsymbol{f}(\boldsymbol{x}) + \boldsymbol{g}(\boldsymbol{x})\boldsymbol{u} \\ \boldsymbol{y} = \boldsymbol{h}(\boldsymbol{x}) \end{cases} \tag{4}$$

where $\boldsymbol{x} \in \boldsymbol{R}^n$ is the state variable, $\boldsymbol{x} \in \boldsymbol{R}^m$ is the input variable, and $f(x, u)$ is the local Leibniz function.

If there is a continuous differentiable positive semidefinite energy storage function $H(x)$ and positive definite function $Q(x)$, for $\forall T > 0$, if the dissipative inequality

$$H[T] - H[0] \le \int_0^T u^T y dt - \int_0^T Q(x)dt \tag{5}$$

holds, the system is strictly passive and $\boldsymbol{u}^{\mathbf{T}}\mathbf{y}$ is the energy power supply rate.

Assuming the total energy function is

$$\boldsymbol{H} = \frac{1}{2}\boldsymbol{x}^{\boldsymbol{T}}\boldsymbol{M}\boldsymbol{x}. \tag{6}$$

Thus, according to (2), the derivative of (6) is derived as follows:

$$\dot{\boldsymbol{H}} = \frac{1}{2}\boldsymbol{x}^{\boldsymbol{T}}\boldsymbol{M}\dot{\boldsymbol{x}} = \frac{1}{2}\boldsymbol{x}^{\boldsymbol{T}}\left[\boldsymbol{u} - \mathbf{J}\boldsymbol{x} - \mathbf{R}\boldsymbol{x}\right]. \tag{7}$$

Because $\boldsymbol{J}$ only reflects the internal situation, which has no influence on the total energy of the system, (7) can be written as

$$\boldsymbol{H}(T) - \boldsymbol{H}(0) = \frac{1}{2}\int_0^T \boldsymbol{x}^{\boldsymbol{T}} u dt. \tag{8}$$

Comparing (8) with (5), this demonstrates that the *LCL*-GCC is passive.

IV. Design of Hybrid PBC-FOSMC Controller

Based on the system state equation obtained earlier and the passivity analysis of the system, a hybrid PBC-FOSMC controller that combines passive control with FOSMC is proposed. In this section, a passive controller is designed to guarantee global stability and ensure strong robustness against external perturbations. Subsequently, the outer-loop FOSMC controller was derived. Finally, the PBC-FOSMC controller and its digitalization are presented.

A. Design of Inner-Loop Passive Controller

Based on the EL equation of the system, the EL equation of the system error can be obtained as

$$\boldsymbol{M}\dot{\boldsymbol{x}}_{\boldsymbol{e}} + \boldsymbol{J}\boldsymbol{x}_{\boldsymbol{e}} + \boldsymbol{R}\boldsymbol{x}_{\boldsymbol{e}} = -\boldsymbol{u} + \boldsymbol{M}\dot{\boldsymbol{x}}_{\boldsymbol{ref}} + \boldsymbol{J}\boldsymbol{x}_{\boldsymbol{ref}} + \boldsymbol{R}\boldsymbol{x}_{\boldsymbol{ref}} \tag{9}$$

where $\boldsymbol{x_e}$ is the system state error given as

$$\begin{aligned}\boldsymbol{x_e} &= \begin{bmatrix} x_{e1} & x_{e2} & x_{e3} & x_{e4} & x_{e5} & x_{e6}\end{bmatrix}^T \\ &= \begin{bmatrix} i_{1\alpha}^* - i_{1\alpha} & i_{1\beta}^* - i_{1\beta} & i_{g\alpha}^* - i_{g\alpha} & i_{g\beta}^* - i_{g\beta} \\ v_{C\alpha}^* - v_{C\alpha} & v_{C\beta}^* - v_{C\beta}\end{bmatrix}^T\end{aligned} \tag{10}$$

where $i_{1\alpha}^*$, $i_{1\beta}^*$, $i_{2\alpha}^*$, $i_{2\beta}^*$, $v_{C\alpha}^*$, and $v_{C\beta}^*$ represent the references of $i_{1\alpha}$, $i_{1\beta}$, $i_{2\alpha}$, $i_{2\beta}$, $i_{C\alpha}$, and $v_{C\beta}$, respectively.

To ensure that the energy function converges quickly, the damping term is added to (9) and the error EL equation after damping is obtained as follows:

$$\boldsymbol{M}\dot{\boldsymbol{x}}_{\boldsymbol{e}} + \boldsymbol{R_d}\boldsymbol{x}_{\boldsymbol{e}} = -\boldsymbol{u} + \boldsymbol{M}\dot{\boldsymbol{x}}_{\boldsymbol{ref}} + \boldsymbol{J}\boldsymbol{x} + \boldsymbol{R}\boldsymbol{x}_{\boldsymbol{ref}} + \boldsymbol{R_a}\boldsymbol{x}_{\boldsymbol{e}} \tag{11}$$

where $\boldsymbol{R_a}$ is the positive definite damping matrix

$$\boldsymbol{R_a} = \begin{bmatrix} r_{a1} & 0 & 0 & 0 & 0 & 0 \\ 0 & r_{a2} & 0 & 0 & 0 & 0 \\ 0 & 0 & r_{a3} & 0 & 0 & 0 \\ 0 & 0 & 0 & r_{a4} & 0 & 0 \\ 0 & 0 & 0 & 0 & r_{a5} & 0 \\ 0 & 0 & 0 & 0 & 0 & r_{a6} \end{bmatrix}. \tag{12}$$

In $\boldsymbol{R_a}$, only r_{a1} and r_{a2} are directly related to the external input and play a role, whereas the other items do not count in damping injection; therefore, $r_{a3} = r_{a4} = r_{a5} = r_{a6} = 0$.

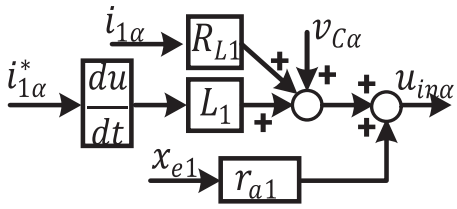

Fig. 2. PBC controller for α-phase.

To ensure that the system reaches a stable state, let the right-hand side of (11) be $\mathbf{0}$

$$\boldsymbol{M}\dot{\boldsymbol{x}}_{\boldsymbol{e}} + \boldsymbol{R_d}\boldsymbol{x}_{\boldsymbol{e}} = \mathbf{0} \tag{13}$$

where $\boldsymbol{R_d}$ is a positive definite matrix, and the energy transfer function of the system is

$$\boldsymbol{H}_{\boldsymbol{e}}(\dot{\boldsymbol{x}}) = \frac{1}{2}\boldsymbol{x}_{\boldsymbol{e}}^{\boldsymbol{T}}\mathbf{M}\dot{\boldsymbol{x}}_{\boldsymbol{e}} = -\frac{1}{2}\boldsymbol{x}_{\boldsymbol{e}}^{\boldsymbol{T}}\boldsymbol{R_d}\boldsymbol{x}_{\boldsymbol{e}} \le 0. \tag{14}$$

If (14) is satisfied, the input of the system is

$$\boldsymbol{u} = \boldsymbol{M}\dot{\boldsymbol{x}}_{\boldsymbol{ref}} + \boldsymbol{J}\boldsymbol{x} + \boldsymbol{R}\boldsymbol{x}_{\boldsymbol{ref}} + \boldsymbol{R_a}\boldsymbol{x}_{\boldsymbol{e}}. \tag{15}$$

Expanding (15), the control law of the passive controller is given as

$$\begin{cases} u_{in\alpha} = L_1\frac{di_{1\alpha}^*}{dt} + v_{C\alpha} + r_{a1}x_{e1} + R_{L1}i_{1\alpha} \\ u_{in\beta} = L_1\frac{di_{1\beta}^*}{dt} + v_{C\beta} + r_{a2}x_{e2} + R_{L1}i_{1\beta} \end{cases}. \tag{16}$$

According to (16), the realization of the PBC controller for i_α is shown in Fig. 2, and the derivation of the PBC controller for i_β is exactly the same as that of i_α.

In practice, the inclusion of a delay of one sampling period associated with the digital implementation due to the calculation, the control law $u_\alpha^{\mathrm{PBC}}(k)$ cannot be obtained directly, the control law will delay one sampling period [15], [34]. Therefore, there is the control law $u_\alpha^{\mathrm{PBC}}(k) = u_{in\alpha}(k+1)$. $u_\beta^{\mathrm{PBC}}(k) = u_{in\beta}(k+1)$. $v_{C\alpha}(k+1)$ and $v_{C\beta}(k+1)$ are delayed by one sampling period T_s due to the sampling delay of the digital controller. Discretizing (16) and considering the digital control delay, with the help of backward Euler discrete method [35], [36], the control law of the passive controller is given as follows:

$$\begin{cases} u_\alpha^{\mathrm{PBC}}(k) = \frac{L_1}{T_s}\left(i_{1\alpha}^*(k) - i_{1\alpha}^*(k-1)\right) + v_{C\alpha}(k+2) \\ \qquad\qquad +r_{a1}x_{e1}(k+1) + R_{L1}i_{1\alpha}(k+2) \\ u_\beta^{\mathrm{PBC}}(k) = \frac{L_1}{T_s}\left(i_{1\beta}^*(k) - i_{1\beta}^*(k-1)\right) + v_{C\beta}(k+2) \\ \qquad\qquad +r_{a2}x_{e2}(k+1) + R_{L1}i_{1\beta}(k+2) \end{cases}. \tag{17}$$

B. Design of Outer-Loop FOSMC Controller

For the converter-side current control, its tracking error at instant k is $x_e(k) = i_1^*(k) - i_1(k)$. Similarly, due to the sampling delay of the digital controller in practice, if the error is defined by $x_e(k)$, the control law $u_C(k)$ will contain $x_e(k+1)$ and $i_1^*(k+2)$. To solve this problem, $x_e(k)$ can be approximately changed to $x_{e1}(k) = i_1^*(k-1) - i_1(k+1)$ with two sampling delays [15], [34].

Because the *LCL*-GCC system with the SMC controller exhibits a chattering phenomenon in the process of convergence along the sliding surface, which easily deteriorates the performance of the control system, the introduction of a fractional-order term in the sliding surface can alleviate the chattering when the system approaches the sliding surface. Similarly, considering the calculation delay to avoid the state quantity at instant $k+1$ in the control law u_α^{PBC} and u_β^{PBC}, moving the fractional-order term $D^\lambda x_e(k)$ forward by one sampling period, and the fractional-order sliding surface is given as follows:

$$\begin{cases} s_1(k) = k_{p1}x_{e1}(k) + k_{d1}D^\lambda x_{e1}(k-1) \\ s_2(k) = k_{p2}x_{e2}(k) + k_{d2}D^\lambda x_{e2}(k-1) \end{cases} \tag{18}$$

where k_{p1}, k_{p2}, k_{d1}, and k_{d2} are the parameters in PBC-FOSMC; k_{p1} and k_{p2} are the coefficients of the proportional term in the fractional sliding surface; k_{d1} and k_{d2} are the coefficients of the fractional derivative term in the sliding surface. In (18), $x_{e1}(k) = i_{1\alpha}^*(k-1) - i_{1\alpha}(k+1)$ and $x_{e2}(k) = i_{1\beta}^*(k-1) - i_{1\beta}(k+1)$; and the two sliding surfaces (s_1 and s_2) are used for $i_{1\alpha}$ and $i_{1\beta}$ control.

The inverter current $i_{1\alpha}(k+1)$ and $i_{1\beta}(k+1)$ cannot be obtained by sampling at instant k. Therefore, the discretization of (1) can be obtained as

$$\begin{cases} i_{1\alpha}(k+1) - \left(1 - \frac{R_{L1}T_s}{L_1}\right) i_{1\alpha}(k) = -\frac{T_s}{L_1}v_{C\alpha}(k) + \frac{T_s}{L_1}u_{in\alpha}(k) \\ i_{g\alpha}(k+1) - \left(1 - \frac{R_{L2}T_s}{L_2}\right) i_{g\alpha}(k) = \frac{T_s}{L_2}v_{C\alpha}(k) - \frac{T_s}{L_2}v_{g\alpha}(k) \\ v_{C\alpha}(k+1) - v_{C\alpha}(k) = \frac{T_s}{C_f}i_{1\alpha}(k) - \frac{T_s}{C_f}i_{g\alpha}(k) \end{cases} \tag{19}$$

Substitute (19) into (18), and the switching functions $s_1(k)$ and $s_2(k)$ can be obtained

$$\begin{cases} s_1(k) = k_{p1}\left(i_{1\alpha}^*(k-1) - \left(1 - \frac{R_{L1}T_s}{L_1}\right) i_{1\alpha}(k) + \frac{T_s}{L_1}v_{C\alpha}(k) \right. \\ \qquad \left. - \frac{T_s}{L_1}u_{in\alpha}(k)\right) + k_{d1}D^\lambda x_{e1}(k-1) \\ s_2(k) = k_{p2}\left(i_{1\beta}^*(k-1) - \left(1 - \frac{R_{L1}T_s}{L_1}\right) i_{1\beta}(k) + \frac{T_s}{L_1}v_{C\beta}(k) \right. \\ \qquad \left. - \frac{T_s}{L_1}u_{in\beta}(k)\right) + k_{d2}D^\lambda x_{e2}(k-1) \end{cases} \tag{20}$$

To ensure that the system can reach the sliding surface from any initial state, the discrete reaching law is designed as follows:

$$\begin{cases} s_1(k+1) - s_1(k) = -T_s\varepsilon_1 \mathrm{sign}\left(s_1(k)\right) - T_s k_1 s_1(k) \\ s_2(k+1) - s_2(k) = -T_s\varepsilon_2 \mathrm{sign}\left(s_2(k)\right) - T_s k_2 s_2(k) \end{cases} \tag{21}$$

Combining (18) and (20), (21) can be written as

$$\begin{cases} s_1(k+1) - s_1(k) = k_{p1}\left(x_{e1}(k+1) - i_{1\alpha}^*(k-1) \right. \\ \quad \left. + \left(1 - \frac{R_{L1}T_s}{L_1}\right) i_{1\alpha}(k)\right) + k_{p1}\frac{T_s}{L_1}\left(u_{in\alpha}(k) - v_{C\alpha}(k)\right) \\ \quad + k_{d1}D^\lambda x_{e1}(k) - k_{d1}D^\lambda x_{e1}(k-1) \\ s_2(k+1) - s_2(k) = k_{p2}\left(x_{e2}(k+1) - i_{1\beta}^*(k-1) \right. \\ \quad \left. + \left(1 - \frac{R_{L1}T_s}{L_1}\right) i_{1\beta}(k)\right) \\ \quad + k_{p2}\frac{T_s}{L_1}\left(u_{in\beta}(k) - v_{C\beta}(k)\right) + k_{d2}D^\lambda x_{e2}(k) \\ \quad - k_{d2}D^\lambda x_{e2}(k-1) \end{cases} \tag{22}$$

Combining the reaching law (21) with (22), the state with sliding mode characteristics can be obtained as

$$\begin{cases} x_{e1}(k+1) = \frac{1}{k_{p1}}(-k_{d1}D^\lambda x_{e1}(k) + k_{d1}D^\lambda x_{e1}(k-1) \\ \qquad -T_s\varepsilon_1 \mathrm{sign}(s_1(k)) - T_s k_1 s_1(k)) + i_{1\alpha}^*(k-1) \\ \qquad -(1 - \frac{R_{L1}T_s}{L_1})i_{1\alpha}(k) + \frac{T_s}{L_1}v_{C\alpha}(k) - \frac{T_s}{L_1}u_{in\alpha}(k) \\ x_{e2}(k+1) = \frac{1}{k_{p2}}(-k_{d2}D^\lambda x_{e2}(k) + k_{d2}D^\lambda x_{e2}(k-1) \\ \qquad -T_s\varepsilon_2 \mathrm{sign}(s_2(k)) - T_s k_2 s_2(k)) + i_{1\beta}^*(k-1) \\ \qquad -(1 - \frac{R_{L1}T_s}{L_1})i_{1\beta}(k) + \frac{T_s}{L_1}v_{C\beta}(k) - \frac{T_s}{L_1}u_{in\beta}(k) \end{cases} \tag{23}$$

C. Design of PBC-FOSMC Controller

The PBC-FOSMC is further improved in PBC. The introduction of SMC causes the system to remain passive, and the system state can converge along the sliding surface, further improving the robustness of the system. The introduction of fractional-order theory can suppress system chattering; thus, the performance of the system is further improved. Fig. 3 shows the control chart of the PBC-FOSMC in α-phase, in which the PBC controller is used as the main body. The original input x_{e1} of the PBC is passed through the sliding surface, as shown in the FOSMC of Fig. 3, such that the system state x_{e1} converges to the equilibrium point along the sliding surface, and the FOSMC output x_{e1}^* is input into the PBC. By inheriting the merits of the PBC and FOSMC controllers, the PBC-FOMSC controller has passive features and can realize SMC with much smaller chattering.

As a result, the proposed PBC-FOSMC method can achieve good dynamic response and strong robustness.

According to Section B in the Appendix, the fractional differential operator is calculated based on its definition, and the fractional differential operator with sample number $n = 50$ for $\lambda = 0.5$ is given by (A7) for approximation. Substitute (19) and (23) into (17), and combine (A7), the discrete PBC-FOSMC law can be obtained as (24) shown at the bottom of the next page.

V. Stability and Arrival Time Analysis

A. Stability Analysis

In the previous section, the passivity of the system was demonstrated using the energy function $\boldsymbol{H_e}(x)$. In this system, the energy function $\boldsymbol{H_e}(x)$ converges through an appropriate damping injection so that the system state can converge to the expected value and ensure the stability of the passive control system. After introducing the SMC theory, the system state converges along the sliding surface. In this section, we demonstrate its reachability.

The Lyapunov function is applied to analyze the system stability. Sliding surface s is a function of the system state for *LCL*-GCCs; thus, the system stability can be judged by the Lyapunov function composed of sliding surface s. The positive definite scalar function V was set as a Lyapunov function

$$V(k) = \frac{1}{2}(s_1^2(k) + s_2^2(k)). \tag{25}$$

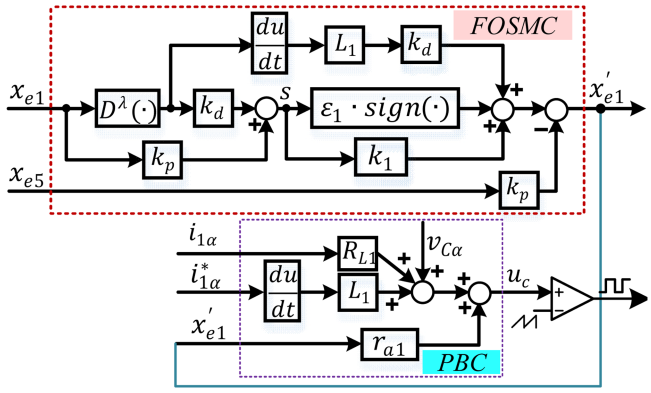

Fig. 3. Realization of PBC-FOSMC controller.

Thus, the derivative of V can be obtained as

$$\dot{V}(k) = s_1(k)\dot{s}_1(k)+s_2(k)\dot{s}_2(k). \tag{26}$$

The system in (25) would be stable if (27) is satisfied

$$\begin{cases} s_1^2(k+1)-s_1^2(k) < 0, s_1(k) \neq 0 \\ s_2^2(k+1)-s_2^2(k) < 0, s_2(k) \neq 0 \end{cases}. \tag{27}$$

Substituting (17) and (18) into (27), $\dot{V}$ can be derived as follows:

$$\begin{aligned} \dot{V}(k) &= \frac{1}{T_s}\left(V(k+1)-V(k)\right) \\ &= s_1(k)(-k_1T_s s_1(k) - T_s\varepsilon_1 \text{sign}(s_1(k))) \\ &\quad +s_2(k)(-k_2T_s s_2(k) - k_2T_s \text{sign}(s_2(k))) \end{aligned} \tag{28}$$

which can be simplified as

$$\begin{cases} -k_1 s_1^2(k) - \varepsilon_1 |s_1(k)| \leq 0 \\ -k_2 s_2^2(k) - \varepsilon_2 |s_2(k)| \leq 0 \end{cases}. \tag{29}$$

It can be obtained from (28) and (29) that

$$\Delta V \leq 0. \tag{30}$$

Because $k_1 > 0$, $k_2 > 0$, $\varepsilon_1 > 0$, and $\varepsilon_2 > 0$. According to the Lyapunov stability theorem, it can be determined from (30) that the system is stable.

B. Arrival Time Analysis

In Section IV-B, it is found that the system is stable under the reaching law (19), and to derive the arrival time to the sliding surface, Lemma 1 defined in [37] is applied.

Lemma 1: For a Lyapunov function $V(x)$, assuming that its initial value is V_0, if there is an inequality of (31) satisfying

$$\dot{V}(x) + \varepsilon V(x) + \mu V^{\sigma}(x) \leq 0 \tag{31}$$

where $\varepsilon, \mu,$ and σ are real numbers and $\varepsilon, \mu > 0, 0 < \sigma < 1$, then for the Lyapunov function satisfying (31), the arrival time is given as

$$T_a \leq \frac{1}{\varepsilon(1-\sigma)} \ln\left(1 + \frac{\varepsilon V_0^{1-\sigma}}{\mu}\right). \tag{32}$$

Then, we can construct a function $f(\varepsilon, \mu, \sigma)$ given as

$$f(\varepsilon, \mu, \sigma) = \frac{1}{\varepsilon(1-\sigma)} \ln\left(1 + \frac{\varepsilon V_0^{1-\sigma}}{\mu}\right). \tag{33}$$

According to Lemma 1, the arrival time of the system state to the sliding surface is satisfied

$$\dot{V}(s) + \varepsilon \text{V}(s) + \mu V^{\sigma}(s) \leq 0. \tag{34}$$

Substituting (18) into (34), inequality (35) can be derived as

$$\underbrace{s\left(-k_1 s - k_2 \text{sig}(s)^b\right)}_{\dot{s}} + \frac{\varepsilon}{2}s^2 + \mu\left(\frac{1}{2}s^2\right)^{\sigma} \leq 0. \tag{35}$$

$$\begin{cases} u_{\alpha}^{\text{PBC}}(k) = \left[L_1 \frac{i^*_{1\alpha}(k)-i^*_{1\alpha}(k-1)}{T_s} + \left(\frac{r_{a1}T_s}{L_1} - \frac{T_s^2}{C_f L_1} - \frac{T_s^2}{C_f L_2} + \left(1 - \frac{R_{L1}T_s}{L_1}\right)^2\right) v_{C\alpha}(k) \right. \\ \quad + \left(\left(1 - \frac{R_{L1}T_s}{L_1}\right)\frac{2T_s}{C_f} - \left(1 - \frac{R_{L1}T_s}{L_1}\right) r_{a1} + \left(1 - \frac{R_{L1}T_s}{L_1}\right)^2 R_{L1}\right) i_{1\alpha}(k) + r_{a1} i^*_{1\alpha}(k-1) \\ \quad + \left(\frac{T_s^2}{C_f L_1} - \frac{r_{a1}T_s}{L_1} + \left(1 - \frac{R_{L1}T_s}{L_1}\right)\frac{R_{L1}T_s}{L_1}\right) u_{in\alpha}(k) + \left(\frac{R_{L1}T_s^2}{C_f L_1} + \frac{R_{L2}T_s^2}{C_f L_2} - 2\frac{T_s}{C_f}\right) i_{g\alpha}(k) + \frac{T_s^2}{C_f L_2} v_{g\alpha}(k) \\ \quad \left. + \frac{-\frac{r_{a1}k_{d1}}{T_s^{\lambda}}\sum_{j=0}^{50} c_j x_{e1}(k-j) + \frac{r_{a1}k_{d1}}{T_s^{\lambda}}\sum_{j=0}^{50} c_j x_{e1}(k-1-j)}{k_{p1}} + \frac{-r_{a1}T_s\varepsilon_1 \text{sign}(s_1(k)) - r_{a1}T_s k_1 s_1(k)}{k_{p1}} \right] \frac{L_1}{L_1 - R_{L1}T_s} \\ u_{\beta}^{\text{PBC}}(k) = \left[L_1 \frac{i^*_{1\beta}(k)-i^*_{1\beta}(k-1)}{T_s} + \left(\frac{r_{a2}T_s}{L_1} - \frac{T_s^2}{C_f L_1} - \frac{T_s^2}{C_f L_2} + \left(1 - \frac{R_{L1}T_s}{L_1}\right)^2\right) v_{C\beta}(k) \right. \\ \quad + \left(\left(1 - \frac{R_{L1}T_s}{L_1}\right)\frac{2T_s}{C_f} - \left(1 - \frac{R_{L1}T_s}{L_1}\right) r_{a2} + \left(1 - \frac{R_{L1}T_s}{L_1}\right)^2 R_{L1}\right) i_{1\beta}(k) + r_{a2} i^*_{1\beta}(k-1) \\ \quad + \left(\frac{T_s^2}{C_f L_1} - \frac{r_{a1}T_s}{L_1} + \left(1 - \frac{R_{L1}T_s}{L_1}\right)\frac{R_{L1}T_s}{L_1}\right) u_{in\beta}(k) + \left(\frac{R_{L1}T_s^2}{C_f L_1} + \frac{R_{L2}T_s^2}{C_f L_2} - 2\frac{T_s}{C_f}\right) i_{g\beta}(k) + \frac{T_s^2}{C_f L_2} v_{g\beta}(k) \\ \quad \left. + \frac{-\frac{r_{a2}k_{d2}}{T_s^{\lambda}}\sum_{j=0}^{50} c_j x_{e2}(k-j) + \frac{r_{a2}k_{d2}}{T_s^{\lambda}}\sum_{j=0}^{50} c_j x_{e2}(k-1-j)}{k_{p2}} + \frac{-r_{a2}T_s\varepsilon_2 \text{sign}(s_2(k)) - r_{a2}T_s k_2 s_2(k)}{k_{p2}} \right] \frac{L_1}{L_1 - R_{L1}T_s} \end{cases}. \tag{24}$$

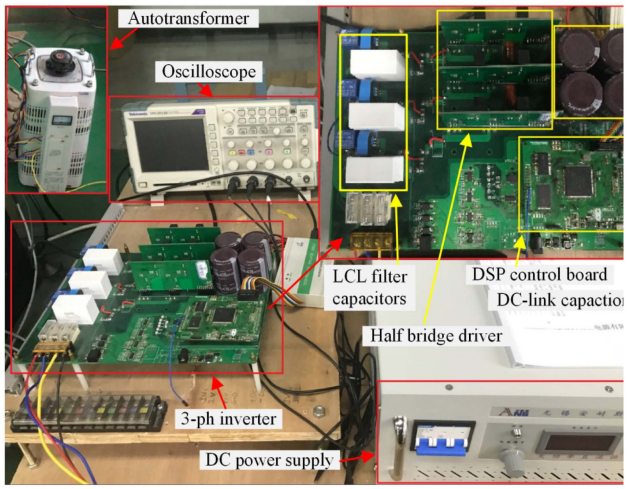

Fig. 4. Experimental setup and designed *LCL*-GCCs.

Inequality (35) can be further simplified as

$$\left(\frac{\varepsilon}{2}-k_1\right)|s|^2-k_2|s|^{b+1}+\frac{\mu}{2^\sigma}|s|^{2\sigma}\leq 0. \tag{36}$$

The minimum $f_{\min}(\varepsilon,\mu,\sigma)$ of (36) can be calculated when $\varepsilon,\mu,$ and σ satisfy

$$(\varepsilon,\mu,\sigma)\in\left\{(\varepsilon,\mu,\sigma)\,|\,\left(\frac{\varepsilon}{2}-k_1\right)|s|^2-k_2|s|^{b+1}+\frac{\mu}{2^\sigma}|s|^{2\sigma}\leq 0\right\}. \tag{37}$$

Thus, the arrival time T_a can be obtained as

$$T_a\leq f_{\min}(\varepsilon,\mu,\sigma). \tag{38}$$

However, the calculation of $f_{\min}(\varepsilon,\mu,\sigma)$ is complicated; therefore, only one set of (ε,μ,σ) satisfying (37) is needed. From (38), $(\varepsilon,\mu,\sigma)=(k_1/4,2^{(b+1)/2}k_2,0.5(b+1))$ is a sufficient and unnecessary condition of (38). Therefore, the arrival time T_a is given by Lemma 1 as

$$T_a\leq\frac{8}{k_1(1-b)}\ln\left(1+\frac{k_1}{4}\cdot\frac{V_0^{\frac{1-b}{2}}}{2^{\frac{b+1}{2}}k_2}\right). \tag{39}$$

VI. Experimental Analysis

In this section, the validity of the proposed PBC-FOSMC control for the *LCL*-GCC is studied.

A. Hardware Setup

To validate the utility of the proposed method, a hardware prototype of 10-kVA three-phase two-level *LCL*-GCCs was set up in the laboratory. The hardware platform is illustrated in Fig. 4. The proposed control scheme was implemented by Texas Instruments 32-b floating-point digital signal processor TMS320F28335PGF, which is widely used in fast and complex mathematical calculations and control algorithms. The power inverter consists of a power transistor and IMZ120R045M1. All power MOSFETs are driven by the isolation driver 1ED20I12FA2. Six Hall current sensors (HCS-LTS-06A) were used for these measurements.

For grid and filter capacitor voltage sampling, a high-precision series voltage divider and a full differential isolation amplifier ACPL-C790 with 0.5% high gain accuracy, 0.05% excellent linearity, and 200-kHz wide-bandwidth were used. Since the output voltage ranges from −1.5 to 1.5 V, a forward-bias voltage circuit with a single-supply and rail-to-rail operational amplifier OPA4340 is used to convert −1.5 to 1.5 V into 0 to 3 V. This allows the system to connect to the ADC port of the microprocessor.

To verify the effectiveness of the proposed controller under weak grid, a grid emulator Chroma 61800 is used in the laboratory, which can be applied to the test of general electrical products (e.g., household appliances, switching power supply). When the object to be tested is a distributed power generation equipment, such as products that will feed back energy to the grid (such as solar inverters, two-way charging, and discharging motors), the 61800 will start the energy recovery mechanism to convert the reverse current/negative power energy generated by the inverter to the ac grid. Unlike ordinary ac power supply, which cannot bear the recharge energy of the object to be tested, the 61800 series can be applied to the full four quadrants in the positive and negative voltage/current positive and negative directions, and has the function of energy recovery, which is sufficient to become a grid emulator.

In the program design for the microprocessor (TMS320F28335), the interrupt routine for the PBC-FOSMC, FOSMC, and SMC control of the *LCL*-GCCs takes approximately 65, 52, and 43 μs, respectively, which are measured by setting the breaking points in the CCS11.0 environment.

B. Test Scenarios

To validate the performance of the proposed method, the PBC-FOSMC controller was compared with the existing FOSMC and SMC methods under five scenarios: 1) steady-state response of the grid current under normal operation, 2) robustness analysis under grid voltage surge, 3) robustness analysis under filter parameter changes, 4) and 5) are the robustness analysis under weak grid and capacitive grid impedance.

The experimental parameters are shown in Table I.

For both the FOSMC and SMC controllers, the sliding surface can be written as $s=x_1+k_1x_2+k_2x_3$. The control laws of the FOSMC and SMC controllers are described as follows.

1) The continuous-time fractional sliding surface of the FOSMC controller is given as $s_{\alpha\beta}=x_{1\alpha\beta}+k_1x_{2\alpha\beta}+k_2x_{3\alpha\beta}+k_3D^\lambda x_{1\alpha\beta}$, thus its control law can be derived as

$$u_{c\alpha\beta}^{\text{FOSMC}}=L_1\dot{i}_{g\alpha\beta}+C_fL_1\ddot{v}_{g\alpha\beta}+C_fL_1L_2\dddot{i}_{2\alpha\beta}^*+v_{C\alpha\beta}-\frac{C_fL_1L_2(x_{2\alpha\beta}+k_1x_{3\alpha\beta}+k_3D^\lambda x_{2\alpha\beta})}{k_2}-L_1C_fL_2\left(-k_4s_{\alpha\beta}-k_5\text{sign}(s_{\alpha\beta})\right). \tag{40}$$

Thus, with the help of backward Euler discrete method [35], [36] and (A7) in the Appendix, the discrete-time control law of (40) is given as (42) shown at the bottom of the this page.

TABLE I
PARAMETER SPECIFICATIONS

Parameters	Symbol	Value
DC voltage	u_{dc}	$700\ V$
Inverter-inductance	R_{L1}, L_1	$0.2\ m\Omega, 2.0\ mH$
Grid-side inductance	R_{L2}, L_2	$0.1 m\Omega, 1\ mH$
Filter capacitance	C_f	$4\ \mu F$
Grid voltage	v_g	$311\ V, 50\ Hz$
Grid current Reference	i_{ref}	$10\ A, 50\ Hz$
Switching and sampling frequency	f_s, f_{samp}	$10\ kHz, 20\ kHz$
Sliding surface of PBC-FOSMC	$k_{p1}, k_{p2}, k_{d1}, k_{d2}, \lambda$	10,10,1,1,0.5
Reaching law of PBC-FOSMC	$\varepsilon_1, \varepsilon_2, k_1, k_2$	1,1,100,100
Damping injection	r_{a1}, r_{a2}	500,500
FOSMC	k_1, k_2, k_3, k_4	$1.5e^{-4}, 2.5\ e^{-9}, 0.5, 1e^{-4}$,
SMC	k_3, k_4	$1e^{-4}, 1$

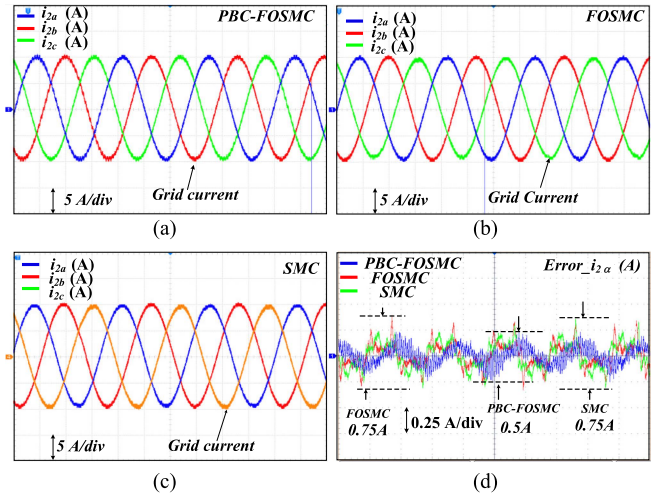

Fig. 5. Waveforms of the steady-state grid current. (a) PBC-FOSMC, (b) FOSMC, and (c) SMC methods. (d) Tracking error ($i_{1\alpha}$) of the grid current under $\alpha\beta$ stationary coordinates.

1) For the SMC controller, its continuous-time sliding surface can be written as $s_{\alpha\beta} = x_{1\alpha\beta} + k_1 x_{2\alpha\beta} + k_2 x_{3\alpha\beta}$, and the control law is

$$u_{c\alpha\beta}^{\text{SMC}} = L_1 \dot{i}_g^{\alpha\beta} + C_f L_1 \ddot{v}_{g\alpha\beta} + C_f L_1 L_2 \dddot{i}_{ref\alpha\beta} + v_{C\alpha\beta} - \frac{C_f L_1 L_2 (x_{2\alpha\beta} + k_1 x_{3\alpha\beta})}{k_2} - L_1 C_f L_2 \left(-k_4 s_{\alpha\beta} - k_5 \text{sign}(s_{\alpha\beta})\right) \tag{41}$$

Similarly, by backward Euler discrete method [35], [36], the discrete-time control law of (41) is given as (43) shown at the bottom of the this page.

Note that in the aforementioned sliding surface and control law, $x_{1\alpha\beta}$ is the grid current error, $x_{2\alpha\beta}$ and $x_{3\alpha\beta}$ are the first and second derivatives of the grid current errors under $\alpha\beta$-frame, expressed as follows:

$$\boldsymbol{x_{1\alpha\beta}} = \begin{bmatrix} i_{g\alpha} - i_{g\alpha}^* \\ i_{g\beta} - i_{g\beta}^* \end{bmatrix}, \boldsymbol{x_{2\alpha\beta}} = \begin{bmatrix} \dot{i}_{g\alpha} - \dot{i}_{g\alpha}^* \\ \dot{i}_{g\beta} - \dot{i}_{g\beta}^* \end{bmatrix},$$

$$\boldsymbol{x_{3\alpha\beta}} = \begin{bmatrix} \ddot{i}_{g\alpha} - \ddot{i}_{g\alpha}^* \\ \ddot{i}_{g\beta} - \ddot{i}_{g\beta}^* \end{bmatrix}, \boldsymbol{x}_g = \begin{bmatrix} \boldsymbol{x_{1\alpha\beta}} & \boldsymbol{x_{2\alpha\beta}} & \boldsymbol{x_{3\alpha\beta}} \end{bmatrix}^T.$$

C. Results and Analysis

1) Steady-State Analysis: Fig. 5(a)–(c) show the steady-state waveform of the three-phase grid current with different control methods under stiff grid, which indicate that all have good steady-state tracking performance. Fig. 5(d) shows the tracking error of the grid current under α-frame, indicating that the current tracking error with PBC-FOSMC is 0.5 A, which reduces the tracking error by 33% compared with existing FOSMC and SMC methods.

2) Grid Voltage Surge: To evaluate the grid current tracking performance under grid voltage variations, the grid voltage increases to 120% of it rated voltage. Fig. 6(a) shows that in the case of a grid voltage surge, the grid current of the PBC-FOSMC is restored to a new stable tracking state in one cycle after a short oscillation. Fig. 6(c) and (e) show that the current tracking waveforms of the FOSMC and SMC will be distorted and cannot be restored to the normal tracking state under a sudden voltage increase of 20%. Fig. 6(b), (d), and (f) show that the control signal of PBC-FOSMC is still sinusoidal while the control signals of FOSMC and SMC are obvious distorted. Complete distortion of α-phase control signal of FOSMC and both α- and β-phase control signals of SMC. Fig. 6(g) and (h) show the grid current errors under the stationary $\alpha\beta$-coordinate, which shows that the grid current tracking errors of PBC-FOSMC are stable within 0.2 A, which is consistent with that under steady state. The grid current errors of FOSMC are 1.1 and 3.4 A. And the grid current tracking errors with SMC controller are about 1.65 and 14 A, resulting in an obvious distortion. Compared with the FOSMC and SMC methods, the PBC-FOSMC is almost

$$u_{c\alpha\beta}^{\text{FOSMC}}(k) = L_1 \left(\frac{C_f (v_{\alpha\beta}(k) - 2v_{g\alpha\beta}(k-1) + v_{g\alpha\beta}(k-2))}{T_s^2} + \frac{C_f L_2 \left(i_{2\alpha\beta}^*(k) - 3i_{2\alpha\beta}^*(k-1) + 2i_{2\alpha\beta}^*(k-2) - i_{2\alpha\beta}^*(k-3)\right)}{T_s^3} + C_f L_2 \left(-k_4 s_{\alpha\beta}(k) - k_5 \text{sign}\left(s_{\alpha\beta}(k)\right)\right) - \frac{C_f L_2 (x_{2\alpha\beta}(k) + k_1 x_{3\alpha\beta}(k) - \frac{k_3}{T_s^4} \sum_{j=0}^{50} c_j x_{2\alpha\beta}(k-j))}{k_2} + \frac{(i_{g\alpha\beta}(k) - i_{g\alpha\beta}(k-1))}{T_s} \right) + v_{C\alpha\beta}(k) \tag{42}$$

$$u_{c\alpha\beta}^{\text{SMC}}(k) = L_1 \left(\frac{C_f (v_{g\alpha\beta}(k) - 2v_{g\alpha\beta}(k-1) + v_{g\alpha\beta}(k-2))}{T_s} + \frac{C_f L_2 \left(i_{\text{ref}\alpha\beta}^*(k) - 3i_{\text{ref}\alpha\beta}^*(k-1) + 2i_{\text{ref}\alpha\beta}^*(k-2) - i_{\text{ref}\alpha\beta}^*(k-3)\right)}{T_s^3} - \frac{C_f L_2 (x_{2\alpha\beta}(k) + k_1 x_{3\alpha\beta}(k))}{k_2} + C_f L_2 \left(k_4 s_{\alpha\beta}(k) + k_5 \text{sign}\left(s_{\alpha\beta}(k)\right)\right) + \frac{(i_{g\alpha\beta}(k) - i_{g\alpha\beta}(k-1))}{T_s} \right) + v_{C\alpha\beta}(k). \tag{43}$$

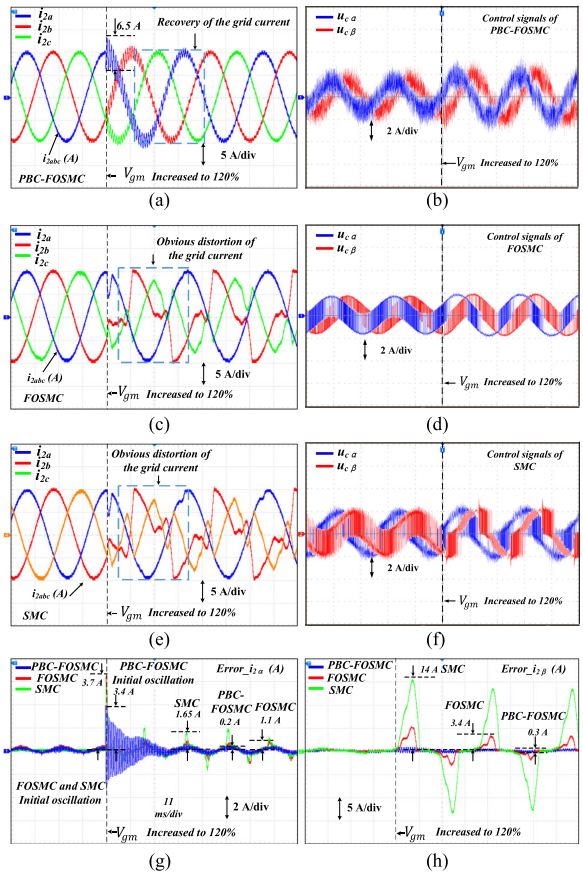

Fig. 6. Grid current tracking under grid voltage surge. (a), (c), and (e) PBC-FOSMC, FOSMC, and SMC. (b), (d), and (f) Control signals of the three methods. (g) and (h) Tracking errors of the grid current (Δi_α and Δi_β).

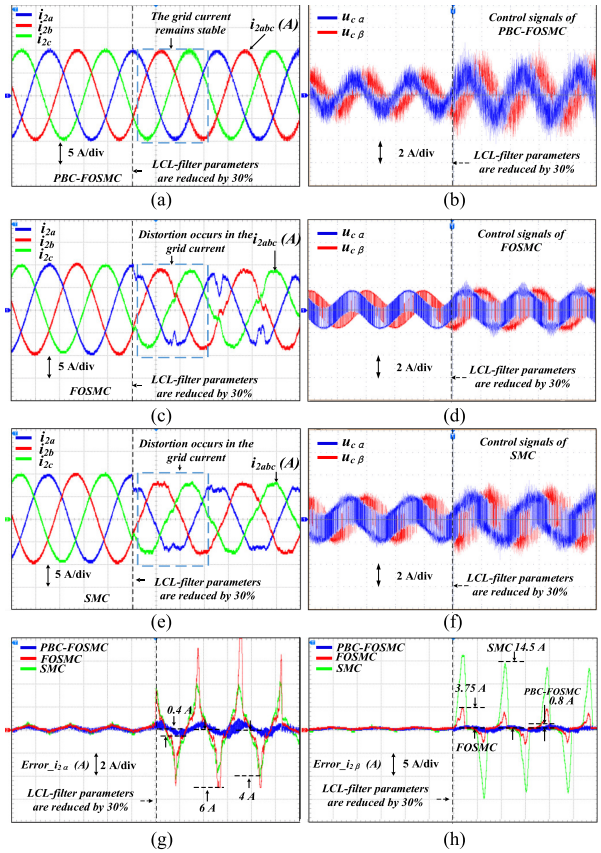

Fig. 7. Grid current under filter parameter variations with different control methods. (a), (c), and (e) PBC-FOSMC, FOSMC, and SMC methods. (b), (d), and (f) Control signals of the three control methods. (g) and (h) Tracking error of i_α and i_β.

unaffected and has good robustness to voltage surge, and the grid current returns to its normal state after a short fluctuation.

3) Filter Parameter Variation: To evaluate the control effect of the PBC-FOSMC under the filter parameter fluctuation, the experiment was carried out when the *LCL* filter parameters are reduced by 30%. Fig. 7 shows the waveforms of the grid current and control signals obtained using the three methods. Fig. 7(a) shows the three-phase grid current with the PBC-FOSMC controller. When the filter parameters change suddenly, the grid current is tracked well and is almost unaffected. Fig. 7(c) and (e) show the grid current with the FOSMC and SMC methods, respectively. After the filter parameter was changed, the grid current was distorted.

Fig. 7(b), (d), and (f) show that the control signals of PBC-FOSMC are still stable while the α-phase control signals of FOSMC and SMC are nonsinusoidal. Fig. 7(g) and (f) show the grid current tracking errors, indicating that the tracking errors of the PBC-FOSMC under the $\alpha\beta$ frame are 0.4 and 0.8 A. Compared with the steady-state condition, the increased error was within 0.5 A compared with the steady-state condition. However, the maximum grid current errors with FOSMC controller are about 6 and 3.75 A, and the grid current errors (Δi_α and Δi_β) with SMC controller are about 4 and 14.5 A. This demonstrates that the PBC-FOSMC exhibits better robustness against filter parameter changes.

4) Weak Grid: With the increase of installed capacity of PV power generation system and the further improvement of PV permeability in recent years, the operation environment of strong grid connected with a large number of PVs increasingly presents the characteristics of weak grid, which is specifically manifested as the large impedance of power grid line and cannot be ignored [38], [39].To evaluate the effect of PBC-FOSMC, FOSMC, and SMC controllers under weak grid, the inverter is changed from a strong grid ($Z_g = 0.157i + 0.3$, the short-circuit ratio (SCR) is 24.2) to a weak grid ($Z_g = 1.57i + 3$, SCR = 2.42) by using the energy recovery grid emulator Chroma 61800. SCR is defined in (44)

$$\mathrm{SCR} = \frac{S_{\mathrm{SC}}}{S_{\mathrm{VSC}}} = \frac{\frac{3}{2}V_{\mathrm{PCC}}^2/|Z_g|}{S_{\mathrm{VSC}}} = \frac{1.5V_{\mathrm{PCC}}^2/\omega_0 L_g}{S_{\mathrm{VSC}}} \tag{44}$$

where S_{SC}, S_{VSC}, V_{PCC}, and Z_g are the short-circuit apparent power of the grid, apparent power of VSC, PCC voltage, and the grid impedance, respectively.

Fig. 8 shows the waveforms of the grid current with three typical methods. Fig. 8(a) shows that the three-phase grid current with PBC-FOSMC is almost unaffected under weak grid, maintaining very small steady-state tracking errors. Fig. 8(b) and (c) show the grid current tracking results with FOSMC and SMC controllers, indicating that the grid current can be well tracked eventually, they all exhibit large oscillations at the

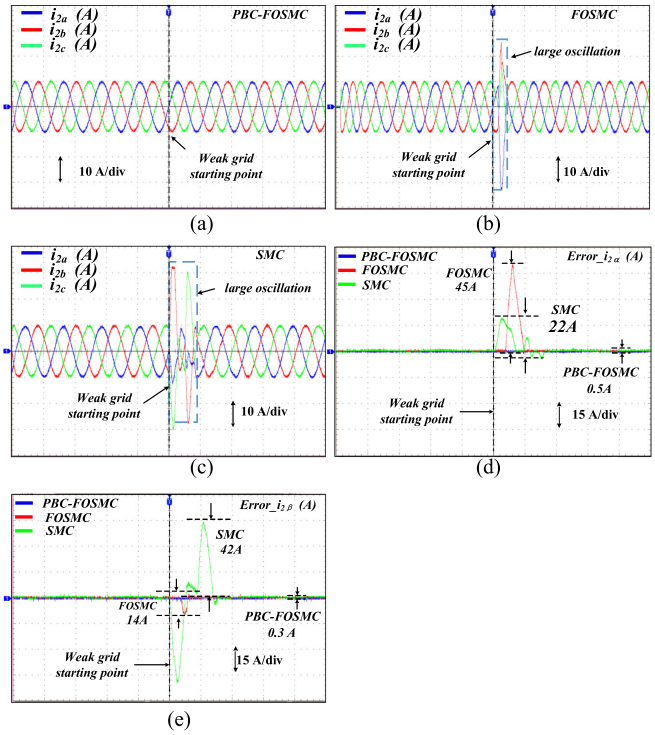

Fig. 8. Grid current tracking under weak grid with different controllers. (a), (b), and (c) PBC-FOSMC, FOSMC, and SMC methods. (d) and (e) Tracking errors of the grid current (Δi_α and Δi_β).

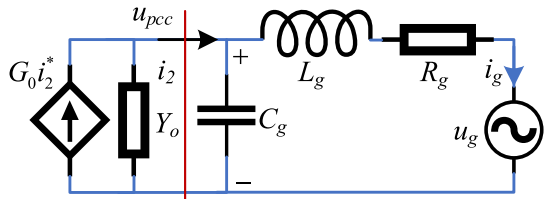

Fig. 9. Equivalent output admittance with various grid impedance type.

beginning. Fig. 8(d) and (e) show the grid current tracking errors under stationary $\alpha\beta$-coordinate, indicating that the grid current tracking errors of PBC-FOSMC are stable within 0.6 A under weak grid, which is very close to 0.5 A under strong grid. The peak grid current tracking errors (Δi_α and Δi_β) of FOSMC before entering steady-state are about 45 and 14 A, whereas those of SMC are about 22 and 42 A. Compared with the other two methods, PBC-FOSMC is almost unaffected and can always maintain excellent tracking performance under weak grid.

5) Capacitive Grid Impedance: In weak grid, long line inductance and transformer leakage inductance play a major role, the grid impedance would be inductive. However, in some cases, the grid impedance may also be capacitive. Fig. 9 shows the equivalent output admittance ($Y0$) of an *LCL*-GCC with various grid impedance types. The *LCL*-GCC can be seen as a current controlled current source. i_2^* is the reference current. R_g, L_g, and C_g represent the resistance, inductance, and capacitance of the grid, respectively. Thus, the grid impedance can be inductive and capacitive. To evaluate the control effect of PBC-FOSMC,

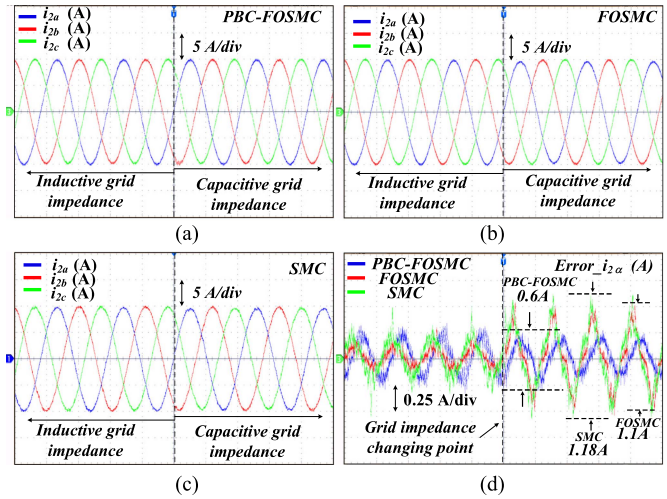

Fig. 10. Waveforms of the steady-state grid current under capacitive grid impedance. (a), (b), and (c) PBC-FOSMC, FOSMC, and SMC methods. (d) Tracking error (i_α) of the grid current under $\alpha\beta$ stationary coordinates.

TABLE II
GRID CURRENT TRACKING PERFORMANCE WITH DIFFERENT CONTROLLERS

Control methods	PBC-FOSMC	FOSMC	SMC
Steady-state error	★★★★	★★★★	★★★★
Grid voltage surge	★★★	★	★
Parameter variation	★★★★	★	★
Weak grid (Inductive impedance)	★★★★	★★	★
Weak grid (Capacitive impedance)	★★★★	★★	★

FOSMC, and SMC controllers under capacitive weak grid, the grid-connected *LCL*-GCC system changes from a weak grid with inductive impedance ($R_g = 3\,\Omega$, $L_g = 5$ mH) to capacitive impedance ($R_g = 3\,\Omega$, $L_g = 5$ mH, $C_g = 3\,\mu$F) by using the programmable energy recovery grid emulator Chroma 61800.

Fig. 10(a)–(c) show the waveforms of the grid current with three typical methods when the grid impedance changes from inductive grid to capacitive grid. Fig. 10(d) shows the tracking error of the grid current under α-frame, indicating that when the grid impedance changes from inductive to capacitive, the tracking error of PBC-FOSMC in α-frame does not change much (0.6 A), whereas the tracking errors of FOSMC and SMC increase to 1.1 and 1.18 A, respectively. Although the three methods can obtain stable tracking performance, the tracking effect of PBC-FOSMC under capacitive weak grid is still much better than the other two control methods, which demonstrates the advantage of the proposed controller.

D. Summary

To clearly show the differences between the PBC-FOSMC, FOSMC, and SMC methods under different scenarios, Table II shows a comparison of the grid current tracking characteristics of PBC-FOSMC, FOSMC, and SMC controllers, indicating that the more red-stars, the better performance the corresponding control method has for grid current tracking under different

test scenarios. Table II clearly demonstrates the superior performance of PBC-FOSMC. It is necessary to note that the complexity of the proposed control method is relatively higher. However, with the development of high-speed microprocessors, the proposed method is of great engineering significance.

VII. Conclusion

In this study, a PBC-FOSMC is proposed for a three-phase *LCL*-GCC system. The controller uses passive control as the main body and makes the system converge along the fractional-order sliding surface, which can effectively improve the system robustness against external perturbations and internal parameter disturbances, and can suppress chattering through the fractional-order term on the sliding surface. To facilitate practical applications, the control law is discretized, and the stability of the system is proved. Experimental results under various conditions have shown that compared with existing methods, the proposed PBC-FOSMC exhibits better robustness and dynamics. In future research, we suggest extending this technique to a motor-drive system.

Appendix

A. Concepts of Fractional-Order Calculus

Fractional calculus is a generalization of the conventional integral calculus. Compared with integral-order calculus, fractional calculus has more universal significance.

There are three common definitions of fractional calculus; Riemann–Liouville (RL), Grunwald–Letnikov (GL), and Caputo [40], which are defined as follows.

1) RL definition

$$ {}_bD_t^{\lambda} f(t) = \frac{1}{\Gamma(n-\lambda)} \frac{d^n}{dt^n} \int_b^t (t-\tau)^{n-\lambda-1} f(\tau) d\tau. \tag{A1} $$

2) GL definition

$$ {}_bD_t^{\lambda} f(t) = \lim_{k\to\infty} k^{-\lambda} \sum_{j=0}^{[b]} (-1)^j \binom{p}{j} f(t-jk). \tag{A2} $$

In (A1) and (A2), $n-1<\alpha<n$. ${}_b{}^{D_t^{\alpha} f(t)}$ is the α-order differential of $f(t)$ when $\alpha>0$, and ${}_b{}^{D_t^{\alpha} f(t)}$ is the $-\alpha$-order integral of $f(t)$ when $\alpha<0$. Γ is the gamma function, k is the calculation step size, and $[b]$ is the rounding function of b.

1) Caputo definition

$$ {}_a^C D_t^p f(t) = \frac{1}{\Gamma(m-a)} \int_a^t \frac{x^{(m)}(\tau)}{(t-\tau)^{a-m+1}} d\tau. \tag{A3} $$

In (A3), $m-1\le a\le m, m\in N$. $\Gamma(p) = \int_0^{+\infty} t^{p-1}e^{-t}dt$ is the gamma function, and p represents any real number.

B. Discrete FOSMC Controller

When fractional order is introduced, chattering in SMPC is suppressed. However, in practical applications, accurate calculation of fractional order often consumes a large amount of computing resources, which increases the cost of the controller. To make the fractional-order SMC easy to realize in the digital controller, the discrete fractional-order SMC law is obtained by approximating the fractional derivative.

Fractional order is defined as follows:

$$ \Delta^{\lambda} x_n = \frac{1}{T_s^{\lambda}} \sum_{j=0}^{\mathrm{n}} (-1)^j \binom{\lambda}{j} x(k-j) \tag{A4} $$

where $\lambda\in$ R is the order of derivation, T_s is the sampling time, and $n\in N$ is the number of samples for which the derivation was computed. The term $\binom{\lambda}{j}$ can be written as

$$ \binom{\lambda}{j} = \begin{cases} 1 & \text{for } j=0 \\ \frac{\lambda(\lambda-1)\cdots(\lambda-j+1)}{j!} & \text{for } j>0 \end{cases}. \tag{A5} $$

And to facilitate writing, note $c_j = (-1)^j \binom{\lambda}{j}$, (A5) can be obtain

$$ \Delta^{\lambda} x_n = \frac{1}{T_s^{\lambda}} \sum_{j=0}^{n} c_j x(n-j). \tag{A6} $$

For this study, if $n=50$ has been used to approximate the fractional derivative, (A6) can be written as

$$ \Delta^{\lambda} x_n = \frac{1}{T_s^{\lambda}} \sum_{j=0}^{50} c_j x(50-j). \tag{A7} $$

After substituting the aforementioned discrete fractional order into the fractional-order control law obtained in the previous section, the discrete fractional-order equivalent SMC law can be obtained.

References

[1] L. Zhou, M. Eull, and M. Preindl, "Optimization-based estimation and model predictive control for high performance, low cost software-defined power electronics," *IEEE Trans. Power Electron.*, vol. 38, no. 1, pp. 1022–1035, Jan. 2023, doi: 10.1109/TPEL.2022.3202863.

[2] N. Moeini, M. Bahrami-Fard, M. Shahabadini, S. M. Azimi, and H. Iman-Eini, "Passivity-based control of single-phase cascaded H-bridge grid-connected photovoltaic inverter," *IEEE Trans. Ind. Electron.*, vol. 70, no. 2, pp. 1512–1520, Feb. 2023, doi: 10.1109/TIE.2022.3165266.

[3] A. Q. Al-Shetwi, M. A. Hannan, K. P. Jern, A. A. Alkahtani, and A. E. Pg Abas, "Power quality assessment of grid-connected PV system in compliance with the recent integration requirements," *Electronics*, vol. 9, no. 2, 2020, Art. no. 366, doi: 10.3390/electronics9020366.

[4] D. Pan, X. Ruan, C. Bao, W. Li, and X. Wang, "Capacitor-current-feedback active damping with reduced computation delay for improving robustness of LCL-type grid-connected inverter," *IEEE Trans. Power Electron.*, vol. 29, no. 7, pp. 3414–3427, Jul. 2014, doi: 10.1109/TPEL.2013.2279206.

[5] H. Komurcugil, S. Ozdemir, I. Sefa, N. Altin, and O. Kukrer, "Sliding-mode control for single-phase grid-connected LCL-filtered VSI with double-band hysteresis scheme," *IEEE Trans. Ind. Electron.*, vol. 63, no. 2, pp. 864–873, Feb. 2016, doi: 10.1109/TIE.2015.2477486.

[6] M. Ben Said-Romdhane, M. W. Naouar, I. Slama-Belkhodja, and E. Monmasson, "Robust active damping methods for LCL filter-based grid-connected converters," *IEEE Trans. Power Electron.*, vol. 32, no. 9, pp. 6739–6750, Sep. 2017, doi: 10.1109/tpel.2016.2626290.

[7] J. K. Li et al., "Research on discretization PI control technology of single-phase grid-connected inverter with LCL filter," *Math. Problems Eng.*, vol. 2014, 2014, Art. no. 129619, doi: 10.1155/2014/129619.

[8] N. Y. Zhang, H. J. Tang, and C. Yao, "A systematic method for designing a PR controller and active damping of the LCL filter for single-phase grid-connected PV inverters," *Energies*, vol. 7, no. 6, pp. 3934–3954, Jun. 2014, doi: 10.3390/en7063934.

[9] W. Jin, Y. L. Li, G. Y. Sun, and L. Z. Bu, "H-infinity repetitive control based on active damping with reduced computation delay for LCL-type grid-connected inverters," *Energies*, vol. 10, no. 5, May 2017, Art. no. 586, doi: 10.3390/en10050586.
[10] Y. B. He, H. S. H. Chung, C. N. M. Ho, and W. M. Wu, "Modified cascaded boundary-deadbeat control for a virtually-grounded three-phase grid-connected inverter with LCL filter," *IEEE Trans. Power Electron.*, vol. 32, no. 10, pp. 8163–8180, Oct. 2017, doi: 10.1109/tpel.2016.2637078.
[11] R. Wu, S. B. Dewan, and G. R. Slemon, "A PWM AC-to-DC converter with fixed switching frequency," *IEEE Trans. Ind. Appl.*, vol. 26, no. 5, pp. 880–885, May 1990, doi: 10.1109/28.60060.
[12] J. Dannehl, C. Wessels, and F. W. Fuchs, "Limitations of voltage-oriented PI current control of grid-connected PWM rectifiers with LCL filters," *IEEE Trans. Ind. Electron.*, vol. 56, no. 2, pp. 380–388, Feb. 2009, doi: 10.1109/TIE.2008.2008774.
[13] K. Seifi and M. Moallem, "An adaptive PR controller for synchronizing grid-connected inverters," *IEEE Trans. Ind. Electron.*, vol. 66, no. 3, pp. 2034–2043, Mar. 2019, doi: 10.1109/TIE.2018.2838098.
[14] G. Shen, X. Zhu, J. Zhang, and D. Xu, "A new feedback method for PR current control of LCL-filter-based grid-connected inverter," *IEEE Trans. Ind. Electron.*, vol. 57, no. 6, pp. 2033–2041, Jun. 2010, doi: 10.1109/TIE.2010.2040552.
[15] R. P. Vieira, L. T. Martins, J. R. Massing, and M. Stefanello, "Sliding mode controller in a multiloop framework for a grid-connected VSI with LCL filter," *IEEE Trans. Ind. Electron.*, vol. 65, no. 6, pp. 4714–4723, Jun. 2018, doi: 10.1109/TIE.2017.2772143.
[16] T. Hornik and Q. Zhong, "A current-control strategy for voltage-source inverters in microgrids based on H-infinity and repetitive control," *IEEE Trans. Power Electron.*, vol. 26, no. 3, pp. 943–952, Mar. 2011, doi: 10.1109/TPEL.2010.2089471.
[17] J. Jung, N. T. Vu, D. Q. Dang, T. D. Do, Y. Choi, and H. H. Choi, "A three-phase inverter for a standalone distributed generation system: Adaptive voltage control design and stability analysis," *IEEE Trans. Energy Convers.*, vol. 29, no. 1, pp. 46–56, Jan. 2014, doi: 10.1109/TEC.2013.2288774.
[18] S. Yang, Q. Lei, F. Z. Peng, and Z. Qian, "A robust control scheme for grid-connected voltage-source inverters," *IEEE Trans. Ind. Electron.*, vol. 58, no. 1, pp. 202–212, Jan. 2011, doi: 10.1109/TIE.2010.2045998.
[19] R. Wai, M. Chen, and Y. Liu, "Design of adaptive control and fuzzy neural network control for single-stage boost inverter," *IEEE Trans. Ind. Electron.*, vol. 62, no. 9, pp. 5434–5445, Sep. 2015, doi: 10.1109/TIE.2015.2408571.
[20] S. Xu, J. Wang, X. Mu, and W. Gu, "Passivity-based control of voltage source PWM rectifier based on synthesis space vector[J]," *Adv. Materials Res.*, vol. 466-467, pp. 1120–1124, 2012.
[21] J. Back and W. Ha, "Robust tracking of robot manipulators via momentum-based disturbance observer and passivity-based controller," *Int. J. Control Automat. Syst.*, vol. 17, no. 4, pp. 976–985, Apr. 2019, doi: 10.1007/s12555-018-0103-0.
[22] C. Y. Chan, "Simplified parallel-damped passivity-based controllers for DC-DC power converters," *Automatica*, vol. 44, no. 11, pp. 2977–2980, Nov. 2008, doi: 10.1016/j.automatica.2008.05.005.
[23] R. Naldi and R. G. Sanfelice, "Passivity-based control for hybrid systems with applications to mechanical systems exhibiting impacts," *Automatica*, vol. 49, no. 5, pp. 1104–1116, May 2013, doi: 10.1016/j.automatica.2013.01.018.
[24] H. Komurcugil, "Improved passivity-based control method and its robustness analysis for single-phase uninterruptible power supply inverters," *IET Power Electron.*, vol. 8, no. 8, pp. 1558–1570, Aug. 2015, doi: 10.1049/iet-pel.2014.0706.
[25] F. X. Wang, G. Y. Lin, and Y. J. He, "Passivity-based model predictive control of three-level inverter-fed induction motor," *IEEE Trans. Power Electron.*, vol. 36, no. 2, pp. 1984–1993, Feb. 2021, doi: 10.1109/tpel.2020.3008915.
[26] Y. I. Son and I. H. Kim, "Complementary PID controller to passivity-based nonlinear control of boost converters with inductor resistance," *IEEE Trans. Control Syst. Technol.*, vol. 20, no. 3, pp. 826–834, May 2012, doi: 10.1109/tcst.2011.2134099.
[27] M. A. Hassan, E. P. Li, X. Li, T. H. Li, C. Y. Duan, and S. Chi, "Adaptive passivity-based control of dc-dc buck power converter with constant power load in dc microgrid systems," *IEEE J. Emerg. Sel. Topics Power Electron.*, vol. 7, no. 3, pp. 2029–2040, Sep. 2019, doi: 10.1109/jestpe.2018.2874449.
[28] J. H. Wang, X. B. Mu, and Q. K. Li, "Study of passivity-based decoupling control of T-NPC PV grid-connected inverter," *IEEE Trans. Ind. Electron.*, vol. 64, no. 9, pp. 7542–7551, Sep. 2017, doi: 10.1109/tie.2017.2677341.
[29] G. Sun, Z. Ma, and J. Yu, "Discrete-time fractional order terminal sliding mode tracking control for linear motor," *IEEE Trans. Ind. Electron.*, vol. 65, no. 4, pp. 3386–3394, Apr. 2018, doi: 10.1109/TIE.2017.2748045.
[30] X. Lin, J. Liu, F. Liu, Z. Liu, Y. Gao, and G. Sun, "Fractional-order sliding mode approach of buck converters with mismatched disturbances," *IEEE Trans. Circuits Syst. I: Reg. Papers*, vol. 68, no. 9, pp. 3890–3900, Sep. 2021, doi: 10.1109/TCSI.2021.3092138.
[31] J. Zhao, M. Huang, H. Yan, C. K. Tse, and X. Zha, "Nonlinear and transient stability analysis of phase-locked loops in grid-connected converters," *IEEE Trans. Power Electron.*, vol. 36, no. 1, pp. 1018–1029, Jan. 2021, doi: 10.1109/TPEL.2020.3000516.
[32] D. Zhu, S. Zhou, X. Zou, and Y. Kang, "Improved design of PLL controller for LCL-type grid-connected converter in weak grid," *IEEE Trans. Power Electron.*, vol. 35, no. 5, pp. 4715–4727, May 2020, doi: 10.1109/TPEL.2019.2943634.
[33] M. Davari and Y. A. R. I. Mohamed, "Robust vector control of a very weak-grid-connected voltage-source converter considering the phase-locked loop dynamics," *IEEE Trans. Power Electron.*, vol. 32, no. 2, pp. 977–994, Feb. 2017, doi: 10.1109/TPEL.2016.2546341.
[34] L. T. Martins, M. Stefanello, H. Pinheiro, and R. P. Vieira, "Current control of grid-tied LCL-VSI with a sliding mode controller in a multiloop approach," *IEEE Trans. Power Electron.*, vol. 34, no. 12, pp. 12356–12367, Dec. 2019, doi: 10.1109/TPEL.2019.2905717.
[35] X. Yang and J. K. Scott, "Accurate uncertainty propagation for discrete-time nonlinear systems using differential inequalities with model redundancy," *IEEE Trans. Autom. Control*, vol. 65, no. 12, pp. 5043–5057, Dec. 2020, doi: 10.1109/TAC.2020.2968241.
[36] S. Li, H. Du, and X. Yu, "Discrete-time terminal sliding mode control systems based on Euler's discretization," *IEEE Trans. Autom. Control*, vol. 59, no. 2, pp. 546–552, Feb. 2014, doi: 10.1109/TAC.2013.2273267.
[37] S. H. Yu, X. H. Yu, B. Shirinzadeh, and Z. H. Man, "Continuous finite-time control for robotic manipulators with terminal sliding mode," *Automatica*, vol. 41, no. 11, pp. 1957–1964, Nov. 2005, doi: 10.1016/j.automatica.2005.07.001.
[38] X. Chen, Y. Zhang, S. Wang, J. Chen, and C. Gong, "Impedance-phased dynamic control method for grid-connected inverters in a weak grid," *IEEE Trans. Power Electron.*, vol. 32, no. 1, pp. 274–283, Jan. 2017, doi: 10.1109/TPEL.2016.2533563.
[39] S. M. Hoseinizadeh, H. Karimi, M. Karimi-Ghartemani, and S. Ouni, "A multivariable phase-locked loop-integrated controller for enhanced performance of voltage source converters under weak grid conditions," *IEEE Trans. Ind. Electron.*, vol. 69, no. 10, pp. 10079–10089, Oct. 2022, doi: 10.1109/TIE.2022.3146607.
[40] C. Li and W. Deng, "Remarks on fractional derivatives," *Appl. Math. Comput.*, vol. 187, no. 2, pp. 777–784, Apr. 2007, doi: https://doi.org/10.1016/j.amc.2006.08.163.

Bo Long (Senior Member, IEEE) received the B.S. degree in electrical engineering from Xi'an Petroleum University, Xian, China, in 2001, and the Ph.D. degree in electrical engineering from Xi'an Jiaotong University, Xi'an, China, in 2008.

He joined the Department of Power Electronics, School of Mechatronics Engineering, University of Electronic Science and Technology of China (UESTC), Chengdu, China, in 2008, and has been promoted to an Associate Professor since 2014. From 2017 to 2018, he was a Visiting Scholar (Guest Postdoctoral Researcher) in the area of renewable energy and microgrids with the Department of Electrical Engineering, Tsinghua University, Beijing, China. He is currently the Supervisor for 11 master's students, two of which have been nominated as provincial outstanding graduate student of UESTC. He has authored more than 20 SCIE-indexed journal papers and one book chapter in the area of power electronics, motor control, battery management system, and smart grid. He has seven issued and ten pending patents. His research interests include ac–dc microgrids, grid-connected converters for renewable energy systems and DGs, model predictive control, power quality, multilevel converters, ac motor control, and resonance suppression technique for smart grid applications.

Dr. Long is an active Reviewer for the IEEE TRANSACTIONS ON POWER ELECTRONICS, *ISA Transactions*, *Applied Energy*, *Energy*, IEEE TRANSACTIONS ON SMART GRID, IEEE TRANSACTIONS ON INDUSTRIAL ELECTRONICS, IEEE TRANSACTIONS ON SUSTAINABLE ENERGY, and IEEE TRANSACTIONS ON ENERGY CONVERSION.

WenZe Mao received the B.S. degree in applied chemistry in 2018 from the School of Materials and Energy, University of Electronic Science and Technology of China, Chengdu, China, where he is currently working toward the M.S. degree in electrical engineering.

His current research interests include model predictive control of paralleled converters, adaptive droop control, model-free predictive control, parameter robustness of power electronic systems, fractional power converter, sliding-mode control, etc.

PengJie Lu received the B.S. degree in mechanical engineering in 2018 from the University of Electronic Science and Technology of China, Chengdu, China, where he is currently working toward the M.S. degree in mechanical engineering.

His research interests include the optimization of ac microgrids, fraction-order controller, sliding-mode control, power distribution, and current circulation suppression between inverters.

Jose Rodriguez (Life Fellow, IEEE) received the Engineer degree in electrical engineering from the Universidad Tecnica Federico Santa Maria, Valparaiso, Chile, in 1977, and the Dr.-Ing. degree in electrical engineering from the University of Erlangen, Erlangen, Germany, in 1985.

Since 1977, he has been with the Department of Electronics Engineering, Universidad Tecnica Federico Santa Maria, where he was a Full Professor and President. Since 2015, he has been the President of the Universidad Andres Bello, Santiago, Chile. He has coauthored two books, several book chapters, and more than 400 journal and conference papers. His research interests include multilevel inverters, new converter topologies, control of power converters, and adjustable-speed drives.

Prof. Rodriguez is a member of the Chilean Academy of Engineering. He was the recipient of the number of Best Paper Awards from journals of the IEEE. In 2014, he was the recipient of the National Award of Applied Sciences and Technology from the government of Chile. In 2015, he was also the recipient of the Eugene Mittelmann Award from the Industrial Electronics Society of the IEEE.

Josep M. Guerrero (Fellow, IEEE) received the B.S. degree in telecommunications engineering, the M.S. degree in electronics engineering, and the Ph.D. degree in power electronics from the Technical University of Catalonia, Barcelona, Spain, in 1997, 2000, and 2003, respectively.

Since 2011, he has been a Full Professor with the Department of Energy Technology, Aalborg University, Aalborg, Denmark, where he is responsible for the Microgrid Research Program. Since 2014, he has been a Chair Professor with Shandong University, Jinan, China; since 2015, he has been a Distinguished Guest Professor with Hunan University, Changsha, China; and since 2016, he has been a Visiting Professor Fellow with Aston University, Birmingham, U.K., and a Guest Professor with the Nanjing University of Posts and Telecommunications, Nanjing, China. In 2019, he became a Villum Investigator by the Villum Fonden, which supports the Center for Research on Microgrids, Aalborg University, being the Founder and Director of the same center. He has authored/coauthored more than 600 journal papers in the fields of microgrids and renewable energy systems, which are cited more than 50 000 times. His research interests are oriented to different microgrid aspects, including power electronics, distributed energy-storage systems, hierarchical and cooperative control, energy management systems, smart metering, the Internet of Things for ac–dc microgrid clusters and islanded microgrids, microgrid technologies applied to offshore wind, maritime microgrids for electrical ships, vessels, ferries, and seaports, and space microgrids applied to nanosatellites and spacecrafts.

Prof. Guerrero is an Associate Editor for a number of IEEE Transactions. He was the recipient of the Best Paper Award for the IEEE TRANSACTIONS ON ENERGY CONVERSION for the period 2014–2015, and the best paper prize of IEEE-PES in 2015. He was also the recipient of the Best Paper Award for the JOURNAL OF POWER ELECTRONICS in 2016. During six consecutive years, from 2014 to 2019, he was awarded by Clarivate Analytics (former Thomson Reuters) as Highly Cited Researcher with 50 highly cited papers. In 2015, he was elevated as IEEE Fellow for his contributions on "distributed power systems and microgrids."

Kil To Chong (Member, IEEE) received the Ph.D. degree in mechanical engineering from Texas A&M University, College Station, TX, USA, in 1995.

He is currently a Professor and the Department Head with the School of Electronics and Information Engineering and a member and the Head of the Advanced Electronics and Information Research Center, Chonbuk National University, Jeonju, South Korea. His research interests include motor fault detection and control, network system control, sensor network systems, time-delay systems, and neural networks.

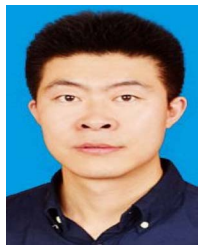

YunLong Teng received the Ph.D. degree in measurement technology and instrument from the University of Electronic Science and Technology of China (UESTC), Chengdu, China, in 2011.

He is currently an Associate Professor with the School of Mechanical and Electrical Engineering, UESTC. His research interests include wide-area measurement, sliding-mode control, and control on renewable power generation systems.